RSC Advances

PAPER

View Article Online
View Journal | View Issue

Cite this: *RSC Adv.*, 2025, **15**, 21678

Heat charge and discharge performance, mechanisms, and reversibility of coupled $LaNi_5$–$La_{0.6}Ce_{0.4}Ni_5$†

Praphatsorn Plerdsranoy,[a] Chonticha Hansongkram,[a] Suwabun Chirachanchai *[b] and Rapee Utke *[a]

A coupled $LaNi_5$–$La_{0.6}Ce_{0.4}Ni_5$ thermochemical heat storage system is proposed for storing waste heat at moderate charging temperatures (≤150 °C) and operating pressure of <30 bar H_2. $LaNi_5$ with lower equilibrium pressure (P_{eq}) and higher reaction enthalpy is used as a high-temperature hydride (HTH) for heat storage, while $La_{0.6}Ce_{0.4}Ni_5$ acts as a low-temperature hydride (LTH) for hydrogen storage. To improve the thermal conductivity and hydrogen diffusion of the hydride beds, the HTH and LTH were doped with 2 wt% multi-walled carbon nanotubes (MWCNTs). Subsequently, HTH and LTH powder samples were packed into two connected cylindrical containers (0.6 kg per container) assembled with a spiral tube heat exchanger. Upon heat charge and discharge cycles, gravimetric and volumetric energy densities reached 122.40 ± 1.37 kJ kg^{-1} and 60.00 ± 0.65 kW h m^{-3}, respectively. During heat discharge, heating and cooling effects were transferred from the hydride beds using a heat transfer fluid. The compatible thermodynamics and kinetics of the HTH and LTH resulted in a comparable heat charge and discharge time (~2 h). This is beneficial for the simple design of thermal storage systems since an extra unit of HTHs or LTHs is not required to optimize the heat exchange reaction rate.

Received 5th January 2025
Accepted 10th June 2025

DOI: 10.1039/d5ra00095e

rsc.li/rsc-advances

1. Introduction

Solar energy is one of the most promising renewable resources; however, it is intermittent in terms of time and season.[1] Thus, thermal energy storage (TES) systems, including sensible heat storage (SHS), latent heat storage (LHS), and thermochemical heat storage (TCHS), have been proposed to obtain continuous and efficient energy from solar power facilities.[2–5] Among these TES systems, TCHS has attracted significant attention owing to its high heat storage density, long-duration storage across seasons with low energy losses, and wide operating temperature ranges.[6–10] TCHS stores and releases thermal energy through reversible chemical reactions of carbonates, hydroxides, magnesium oxide, and metal hydrides.[4,9,11,12] The last category of metal hydride-based TCHS (MH-TCHS) has been recognized as one of the potential candidates for energy conversion since it possesses 5–10-times higher energy density than other TCHS systems[6,13] and up to 7- and 4-times greater energy storage capacity than SHS and LHS, respectively.[14] Since a single reactor of MH-TCHS requires an external hydrogen reservoir and mechanical compressor during heat charge and discharge, a configuration involving two connected metal hydride containers of high- and low-temperature metal hydrides (HTHs and LTHs, respectively) has been widely used.[15] HTHs, which are used for heat storage, have higher reaction enthalpy and lower equilibrium pressure (P_{eq}) than LTHs acting as a hydrogen reservoir.[16,17] Heat charge occurs at HTHs through endothermic dehydrogenation, and concurrently, LTHs absorb hydrogen from HTHs and release low-grade heat. In the case of heat discharge, LTHs desorb hydrogen at room temperature or slightly elevated temperature (~40–50 °C) compared with HTHs. Heat is discharged upon exothermic hydrogenation of HTHs. The amount of stored heat depends on the hydride formation enthalpy of HTHs and hydrogen content exchange between HTHs and LTHs.[18,19]

Several coupled HTH–LTH thermal storage systems of Mg-based hydrides have been reported, such as MgH_2–$LaNi_5$,[19,20] MgH_2–LaNiAl and MgH_2–TiFeMn,[21] Mg_2Ni–$LaNi_5$,[22,23] Mg_2FeH_6–$TiMn_{1.5}$,[24] Mg_2FeH_6–Na_3AlH_6,[25,26] MgH_2, Mg_2FeH_6, $NaMgH_3$, or $NaMgH_2F$ coupled with $Ti_{1.2}Mn_{1.8}$ [27] and Mg-*x* wt% $LaNi_5$ (x = 20 and 30) coupled with $LaNi_{4.7}Al_{0.3}$ or $LaNi_{4.6}Al_{0.4}$.[28] These systems operate at temperatures exceeding 200 °C, which conventional waste heat cannot provide. Thus, pairs of interstitial hydrides de/absorbing hydrogen at lower temperatures have been investigated for thermal storage systems operating at moderate temperatures (≤150 °C). Coupled $LaNi_{4.7}Al_{0.3}$–$LaNi_5$

[a]*School of Chemistry, Institute of Science, Suranaree University of Technology, Nakhon Ratchasima 30000, Thailand. E-mail: rapee.g@sut.ac.th*

[b]*Center of Excellence in Bioresources to Advanced Materials, The Petroleum and Petrochemical College, Chulalongkorn University, Bangkok, 10330, Thailand. E-mail: suwabun.c@chula.ac.th*

† Electronic supplementary information (ESI) available. See DOI: https://doi.org/10.1039/d5ra00095e

absorbed heat at 30–80 °C and possessed the volumetric energy density of 56 kW h m^{-3} with the peak discharge temperature of 70 °C.[29] Different pairs of $LaNi_{(5-x)}Sn_x$–$MmNi_{4.6}Al_{0.4}$ (x = 0.15–0.45) had heat storage and recovery temperatures of 93–140 and 105–165 °C, respectively.[30] The highest theoretical energy density and coefficient of performance (COP) of 129 kJ kg^{-1} and 0.54, respectively, were obtained using $LaNi_{4.65}Sn_{0.35}$-$MmNi_{4.6}Al_{0.4}$. In the case of $LaNi_5$, the effects of substituting (i) Ni with Al or Sn, and (ii) La with Ce on the thermodynamics and heat storage efficiency were studied.[18] The hydrogen ab/desorption performance during heat charge and discharge of the coupled HTH–LTH was related to their different P_{eq} (ΔP_{eq}). At operating temperatures up to 150 °C, the best COP and energy storage density of 0.54 and 243.96 kJ kg^{-1}, respectively, were achieved using the $La_{0.9}C_{0.1}Ni_5$–$LaNi_{4.7}Sn_{0.3}$ pair due to its maximum ΔP_{eq} of 6.09 bar at room temperature. To obtain a heat storage performance with good reaction rate, high operating pressures during energy storage and release of up to 10.37 and 73.48 bar, respectively, were applied. Another hydride pair of $LaNi_{4.25}Al_{0.75}$ and $La_{0.75}Ce_{0.25}Ni_5$ with P_{eq} at 20–40 °C of <0.2 and 4–10 bar, respectively, stored the waste heat at ~150 °C with a relatively low operating pressure (<10 bar) and produced both heating and cooling effects during the discharge process.[15] Because P_{eq} of HTH ($LaNi_{4.25}Al_{0.75}$) was significantly low, at a charging temperature of 150 °C, low hydrogen pressures of ~6.5–7 bar were obtained. The latter was not sufficient for effective hydrogen absorption by LTH ($La_{0.75}Ce_{0.25}Ni_5$), leading to a small hydrogen content exchange between HTH and LTH (~0.42 wt% H_2 with respect to HTH mass). Besides, deficient heating and cooling effects were observed during energy discharge, for example, the heat transfer fluid temperature increased and decreased by only 7.3 °C and 2.4 °C, respectively.

In this study, the coupled $LaNi_5$–$La_{0.6}Ce_{0.4}Ni_5$ is proposed to operate at a charging temperature of 150 °C and moderate pressure of <30 bar H_2. The P_{eq} at 20–30 °C during hydrogen desorption and absorption on $LaNi_5$ as HTH (2.0 and 3.0 bar, respectively[31]) was greater than that of Al-substituted $LaNi_5$ (<0.2 bar).[15] The obtained hydrogen pressure during heat charge of HTH was enhanced, favoring hydrogen absorption by LTH. Given that the heat charge and discharge performance likely depends on the ΔP_{eq} between HTH and LTH, $La_{0.6}Ce_{0.4}Ni_5$ with a high P_{eq} for hydrogen desorption and absorption (10 and 30 bar, respectively, at 40 °C [32]) was selected as LTH. Furthermore, the thermal conductivity and hydrogen diffusion in hydride beds during the heat charge and discharge cycles were improved by doping with multi-walled carbon nanotubes (MWCNTs).[33,34] The thermodynamic properties of LTH and HTH, their heat charge and discharge performance, mechanisms, and cycling stability, as well as the hydrogen content exchange between HTH and LTH were investigated. Also, the heating and cooling effects obtained during heat discharge were characterized.

2. Experiments

As-received $LaNi_5$ and $La_{0.6}Ce_{0.4}Ni_5$ (hydrogen storage grade, Whole Win Materials Sci. & Tech. Co. Ltd, Beijing) were mixed with 2 wt% MWCNTs (99.99%, Nano Generation Co., Ltd). The mixtures of $LaNi_5$-MWCNTs and $La_{0.6}Ce_{0.4}Ni_5$-MWCNTs were

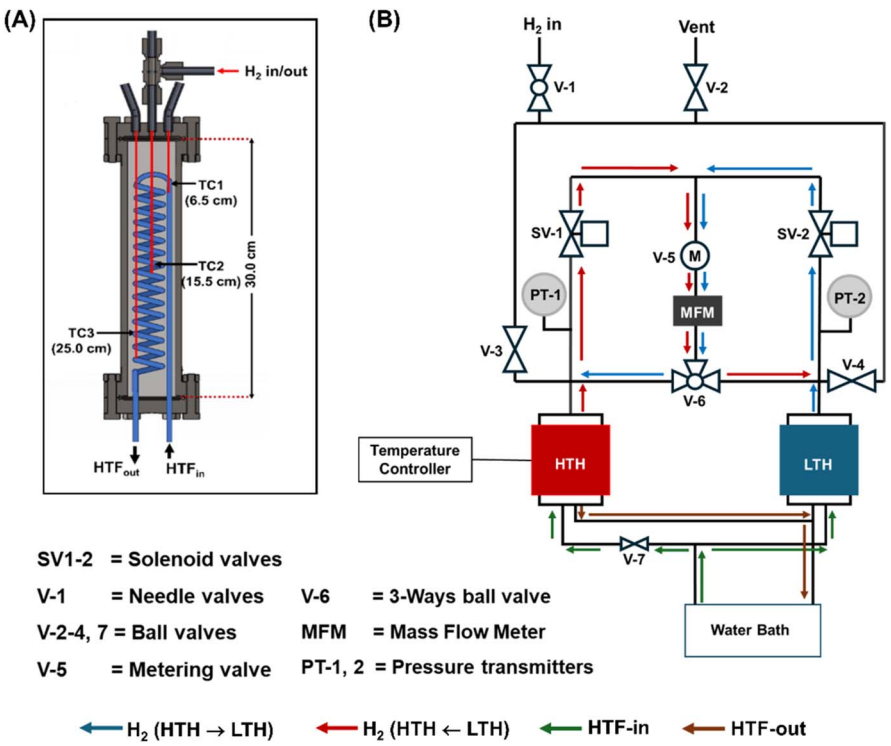

Fig. 1 Schematic diagram of a cylindrical container assembled with a spiral tube heat exchanger and positions of temperature sensors (TCs) for HTH and LTH (A) and the test station for studying heat storage performance (B).

activated by hydrogen absorption and desorption at room temperature (~25 °C) under vacuum and 40 bar H_2. The activated $LaNi_5$-MWCNTs and $La_{0.6}Ce_{0.4}Ni_5$-MWCNTs were used as high- and low-temperature metal hydrides, denoted as HTH and LTH, respectively. The powder samples of HTH (~0.6 kg) and LTH (~0.6 kg) were packed tightly into stainless-steel mesh cylinders (SS304, no. 120) and placed into cylindrical containers (packing volume of ~0.35 mL) equipped with a spiral tube heat exchanger (Fig. 1(A)).

Powder X-ray diffraction (PXD) experiments were carried out using a Bruker D2 PHASER with a Cu K_α radiation ($\lambda = 0.15406$ nm). The powder sample was packed in an airtight sample holder, covered by a poly(methyl methacrylate) (PMMA) dome under an N_2 atmosphere in a glove box. The spectra were collected in the 2θ range of 10–80° at the scanning step of 0.02° s^{-1}. The unit cell parameters of all the samples were analyzed using the TOPAS software with Le Bail structural refinement.

The dehydrogenation kinetics and hydrogen capacities of HTH and LTH were investigated using a carefully calibrated Sievert-type apparatus automatically controlled by software developed in a LabVIEW® environment (Fig. S1 in ESI†).[35–37] The pressure changes during the experiments were detected by a pressure transducer (0–3000 psig, an OMEGA Engineering PX409-3KGI). Dehydrogenation was performed under isothermal conditions at room temperature (~25 °C) and a setting hydrogen flow rate of 2.0 standard L per min (SLM) controlled by a mass flow controller (MFC, a Bronkhorst EL-FLOW selected F-201CV). The temperature, pressure, and mass flow rate profiles were collected and transferred to a computer using an AI2101 module converter datalogger (Wisco). The volume of hydrogen desorbed (standard L, SL) was obtained by integrating the peak area under the hydrogen flow rate (SLM) *versus* time (min) plot. Number of moles of the desorbed hydrogen (n_{H_2}) and hydrogen storage capacity were calculated using the following equations:

$$V_{STP} = \frac{P_s V_s T_{STP}}{T_s P_{STP}} \quad (1)$$

$$n_{H_2} = \frac{V_{STP}}{22.4\ \text{L mol}^{-1}} \quad (2)$$

$$H_2\ \text{capacity(wt\%)} = \frac{n_{H_2} \times 2.016\ \text{g mol}^{-1}}{\text{sample weight}} \times 100, \quad (3)$$

where V_{STP} (L) and V_S (SL) are the volume of hydrogen at the standard temperature and pressure condition (STP, $T_{STP} = 273.15$ K and $P_{STP} = 1.0133$ bar) and at the standard condition of MFC ($T_S = 296.15$ K and $P_S = 1.0156$ bar), respectively. The standard molar volume is 22.4 L mol^{-1}.

The pressure composition isotherms (PCI) during the dehydrogenation of HTH and LTH were recorded using a carefully calibrated test station controlled by software developed in the LabVIEW® environment (Fig. S2 in ESI†).[38] The temperature of the sample holder and furnace during the experiments was detected using K-type thermocouples (−250 °C to 1300 °C, SL heater). The pressure changes during dehydrogenation were recorded using an absolute pressure transducer (0–100 bar, a Kistler). Upon dehydrogenation, the hydrogen pressure was stepwise reduced by 0.2–1 bar per step, and the standard deviation (SD) was set in the range of 0.002–0.01 bar to approach the equilibrium state. The pressure reduction and SD were controlled using MFC (a Bronkhorst EL-FLOW High pressure model F-221M-RAD-22-V). The signals of temperatures, pressures, and mass flow rates were transferred to a computer using an AI2101 module converter datalogger (Wisco). The pressure change (ΔP) in each step was used to calculate number of moles of the desorbed hydrogen (n_{H_2}) (eqn (4)) and hydrogen capacity (eqn (3)). The PCI experiments of HTH were performed at 30–75 °C and 1–20 bar H_2, while that of LTH at 30–60 °C and 1–40 bar H_2.

$$(\Delta P)V = n_{H_2}RT \quad (4)$$

where P and V are hydrogen pressure (bar) and volume of the system (L), respectively. T, n_{H_2}, and R indicate temperature (K), moles of hydrogen (mol), and gas constant (0.08314 L bar K^{-1} mol^{-1}), respectively.

The heat charge and discharge performance and cycling stability of the coupled $LaNi_5$–$La_{0.6}Ce_{0.4}Ni_5$ for 8 cycles were investigated using a laboratory test station (Fig. 1(B)). Three K-type thermocouples were placed in the axial direction of the HTH and LTH containers (TC1–TC3) to measure the sample temperatures during heat charge and discharge reaction (Fig. 1(B)). The pressure changes in HTH and LTH during the experiments were monitored using pressure transmitters (a Kistler) with the operating range of 0–50 and 0–35 bar, respectively. The temperature and pressure signals were transferred to a computer using module data loggers (National Instruments NI USB-6009 and Wisco AI210). Direct-acting plunger solenoid valves (Type 0255, a Bürkert) as well as ball and needle valves (SS316, Swagelok) were used to control the hydrogen flow direction between HTH and LTH during the heat storage cycles. Heat charge was done by heating HTH to the set temperature (T_{set}) of 150 °C at 1 bar H_2. When heat charge was complete, heat discharge was carried out by cooling HTH to room temperature and conducting hydrogen desorption and absorption at LTH and HTH, respectively. Deionized water at room temperature (25–27 °C) with the flow rate of ~15–17 L min^{-1} was used as the heat transfer fluid (HTF) for the HTH and LTH containers. Hydrogen content exchange between HTH and LTH was recorded using a mass flow meter (MFM) (0–3.0 SLM, a Bronkhorst EL-FLOW selected F-201CV). Hydrogen volume (Vs) was obtained by integrating the peak area under the hydrogen flow rate (SLM) *versus* time (min) plot. Hydrogen moles and storage capacities were calculated using eqn (1)–(3).

3. Results and discussion

The phase compositions of the as-prepared samples of HTH ($LaNi_5$-MWCNTs) and LTH ($La_{0.6}Ce_{0.4}Ni_5$-MWCNTs) were characterized using the PXRD technique. As shown in Fig. 2(A(a and c)), the PXRD spectra of the as-received $LaNi_5$ and $La_{0.6}Ce_{0.4}Ni_5$ possess diffraction peaks corresponding to the $CaCu_5$-type hexagonal structure. The diffraction peaks of $La_{0.6}Ce_{0.4}Ni_5$

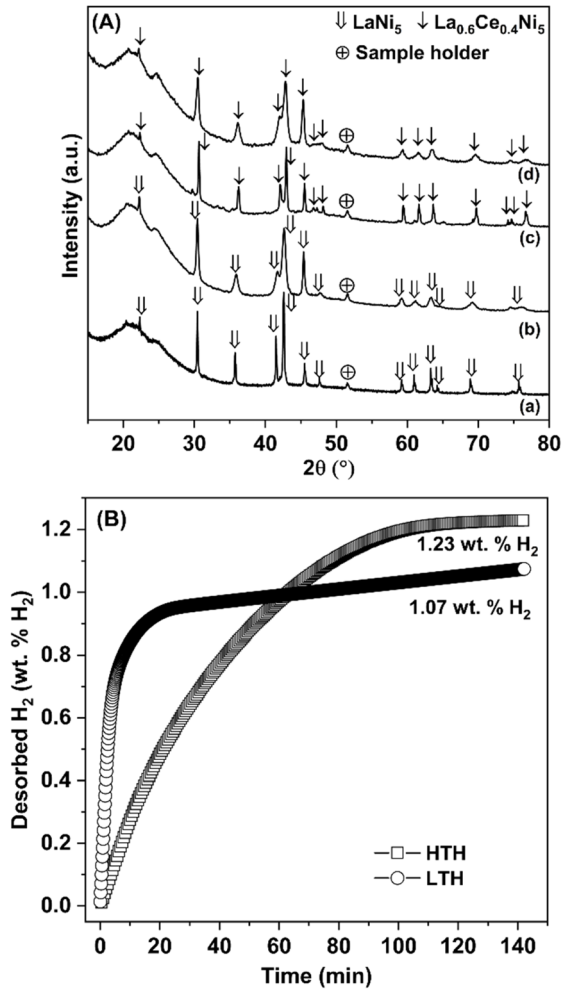

Fig. 2 PXRD patterns (A) of as-received $LaNi_5$ (a), HTH (b), as-received $La_{0.6}Ce_{0.4}Ni_5$ (c), and LTH (d) and dehydrogenation kinetics of HTH and LTH (B).

shifted to greater 2θ values with respect to that of $LaNi_5$, indicating a reduction in its unit cell volume. This is because La in $LaNi_5$ is partially replaced by Ce with a smaller atomic radius. Structural refinements were carried out to investigate the changes in lattice parameters and unit cell volumes of the samples in different states. Fig. S3 in the ESI† reveals the La Bail structural refinements of all the samples, while the lattice parameters and unit cell volumes are summarized in Table 1. The refinement results show that the unit cell volume of $La_{0.6}Ce_{0.4}Ni_5$ (85.441 Å^3) is smaller than that of $LaNi_5$ (86.797 Å^3) (Table 1). In the case of the as-prepared HTH and LTH, broader diffractions than that of the original hydrides (as-received $LaNi_5$ and $La_{0.6}Ce_{0.4}Ni_5$) were observed (Fig. 2(A(b and d))), respectively. This can be explained by the increase in the number of defects and/or microstrain due to the unit cell expansion and contraction regularly found after de-/rehydrogenation upon activation.[37,39] In the structural refinement, the unit cell volumes of the as-prepared HTH and LTH (86.980 and 85.190 Å^3) slightly changed with respect to that of the as-received $LaNi_5$ and $La_{0.6}Ce_{0.4}Ni_5$, respectively (Table 1). Moreover, the

Table 1 Lattice parameters and unit cell volumes of as-received samples of $LaNi_5$ and $La_{0.6}Ce_{0.4}Ni_5$ as well as HTH and LTH in as-prepared state and after cycling

	Lattice parameters		
Samples	a (Å^3)	c (Å)	Volume (Å^3)
As-received $LaNi_5$	5.019	3.979	86.797
As-received $La_{0.6}Ce_{0.4}Ni_5$	4.969	3.996	85.441
As-prepared HTH	5.012	3.998	86.980
As-prepared LTH	4.961	3.997	85.190
HTH after cycling	5.014	3.995	86.970
LTH after cycling	4.962	3.999	85.260

hydrogen capacities and kinetics of HTH and LTH were characterized. Under ambient conditions ($T \sim 25$ °C and $p(H_2) \sim 1$ bar), HTH and LTH released 1.23 and 1.07 wt% H_2, respectively, within 140 min (Fig. 2(B) and Table 2).

According to the de-/rehydrogenation mechanisms (eqn (5) and (6)), the theoretical hydrogen capacities of $LaNi_5$ and $La_{0.6}Ce_{0.4}Ni_5$ are comparable at 1.37 wt% H_2 and those of the HTH and LTH containing 2 wt% MWCNTs are 1.34 wt% H_2. The lower hydrogen capacities of HTH and LTH with respect to the theoretical values might be due to their incomplete activation. In the case of kinetic properties, the dehydrogenation rate of LTH is significantly faster than HTH during 0–60 min (Fig. 2(B)). Given that the hydrogen capacities of HTH and LTH are in the comparable range of 1.1–1.2 wt% H_2 (Fig. 2(B)), the weights of the HTH and LTH powder samples packed in the cylindrical containers are equal (0.6 kg per container).

$$LaNi_{5(s)} + 3H_{2(g)} \leftrightarrow LaNi_5H_{6(s)} \quad (5)$$

$$La_{0.6}Ce_{0.4}Ni_{5(s)} + 3H_{2(g)} \leftrightarrow La_{0.6}Ce_{0.4}Ni_5H_{6(s)} \quad (6)$$

The pressure composition isotherms (PCI) during the dehydrogenation of HTH were investigated at 30–75 °C in the pressure range of 1–20 bar H_2, while that of LTH was done at 30–60 °C in the pressure range of 1–40 bar H_2. According to Fig. 3, the equilibrium pressures (P_{eq}) during hydrogen desorption of HTH are in the range of 2.2–8.9 bar at 30–75 °C, while those of LTH are 7.7–19.3 bar at 30–60 °C. The reversible hydrogen capacities of HTH and LTH are in the range of 0.40–1.10 and 0.50–1.05 wt% H_2, respectively (Fig. 3). The obtained P_{eq} of HTH ($LaNi_5$-MWCNTs) and LTH ($La_{0.6}Ce_{0.4}Ni_5$-MWCNTs) in this study are in accordance with the P_{eq} of $LaNi_5$ and $La_{0.6}Ce_{0.4}Ni_5$ reported in previous investigations.[40,41] Given that the P_{eq} of LTH is greater than that of HTH, the dehydrogenation kinetics

Table 2 Hydrogen storage capacities and reaction enthalpy (ΔH) and entropy (ΔS) during dehydrogenation of as-prepared HTH and LTH

Samples	H_2 storage capacity (wt% H_2)	ΔH (kJ mol^{-1})	ΔS (J K^{-1} mol^{-1})
As-prepared HTH	1.23	27.3	96.7
As-prepared LTH	1.07	25.5	101.1

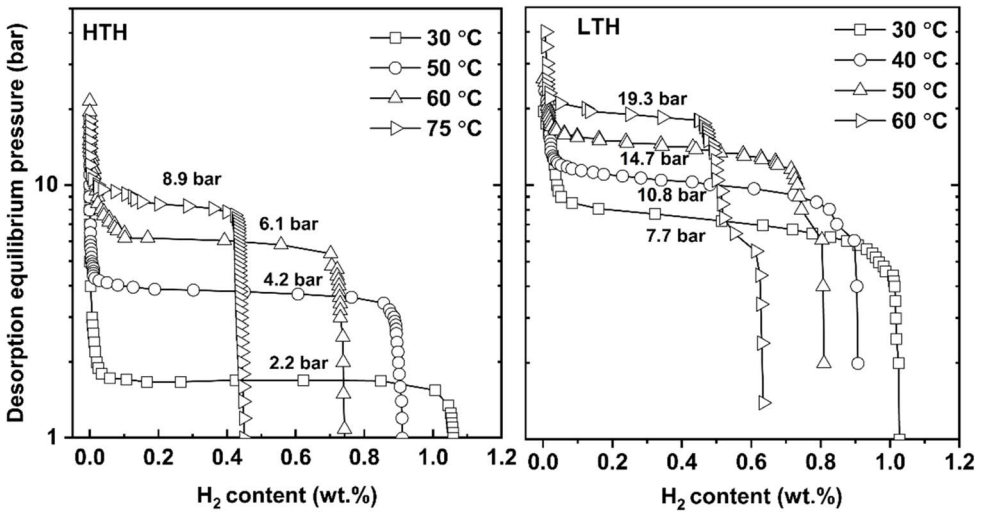

Fig. 3 Pressure composition isotherms (PCI) during dehydrogenation of HTH and LTH.

under ambient conditions ($T \sim 25$ °C and p(H_2)~1 bar) of LTH is significantly faster than that of HTH (Fig. 2(B)). According to the van't Hoff equation (eqn (7)), the reaction enthalpy (ΔH) and entropy (ΔS) of hydride materials can be derived from the plot of $\ln P_{eq}$ *versus* $1/T$.[42] ΔH and ΔS upon the dehydrogenation of HTH are 27.3 kJ mol^{-1} and 96.7 J K^{-1} mol^{-1}, respectively, while that of LTH are 25.5 kJ mol^{-1} and 101.1 J K^{-1} mol^{-1}, respectively (Fig. 4 and Table 2).

$$\ln P_{eq} = -\frac{\Delta H}{RT} + \frac{\Delta S}{R} \quad (7)$$

where R and T are the gas constant (8.314 J mol^{-1} K^{-1}) and temperature (K), respectively.

Furthermore, the heat charge and discharge performance and cycling stability of the coupled $LaNi_5$–$La_{0.6}Ce_{0.4}Ni_5$ during 8 cycles were investigated. Two cylindrical tanks were packed with the HTH and LTH powder samples and three temperature sensors (TC1-TC3) were placed in the axial direction of each tank (Fig. 1(A)). The HTH and LTH-based tanks were assembled with the test station (Fig. 1(B)). Heat charge was carried out by dehydrogenating HTH at 150 °C with the hydrogen flow direction of HTH → LTH. The released hydrogen was absorbed by LTH at room temperature. When the heat charge at HTH and hydrogen absorption at LTH were complete, HTH was cooled to room temperature. Heat discharge was continued by switching the hydrogen flow direction to LTH → HTH. Both hydrogen desorption from LTH and hydrogen absorption on HTH were performed at room temperature. Heating and cooling effects were obtained from exothermic hydrogenation of HTH and endothermic dehydrogenation of LTH. The heat charge and discharge performance as well as cycling stability were characterized by tracking the changes in (i) temperature and pressure of the HTH and LTH tanks (T_{HTH}, T_{LTH}, $P_{H_2\text{-}HTH}$, and $P_{H_2\text{-}LTH}$), (ii) temperature of the heat transfer fluid (T_{HTF}, deionized water at 25–27 °C with the flow rate of ~15–17 L min^{-1}), and (iii) mass flow rate of hydrogen gas (FR-H_2) exchange between HTH and LTH. Fig. 5 shows consistent patterns of temperature, pressure, and H_2-FR upon 8 heat charge and discharge cycles, indicating the cycling stability of the coupled $LaNi_5$–$La_{0.6}Ce_{0.4}Ni_5$ thermal storage system. The results during the 5th cycle were selected to thoroughly study the heat charge and discharge performance and mechanisms.

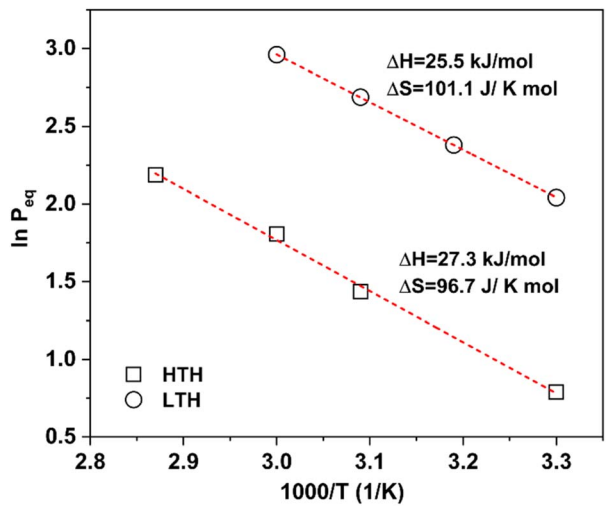

Fig. 4 Van't Hoff plots during dehydrogenation of HTH and LTH.

During heat charge at 150 °C, the temperature of the powder at all positions in the HTH tank (TC1–TC3) increased to 109–150 °C (Fig. 6(A)). The different temperatures observed at TC1–TC3 of HTH can probably be explained by the temperature gradient inside the cylindrical tank due to the poor thermal conductivity of the hydride material. The fine powder of metal hydrides obtained from mechanical forces due to the lattice expansion during the hydrogen ab/desorption cycles led to a dramatic decrease in effective thermal conductivity.[43,44] According to Fig. 6(A), the heat charge (or endothermic dehydrogenation) of HTH was observed from the slight interruption during the increase in temperature at TC1 and TC2 (t = 31–31.5

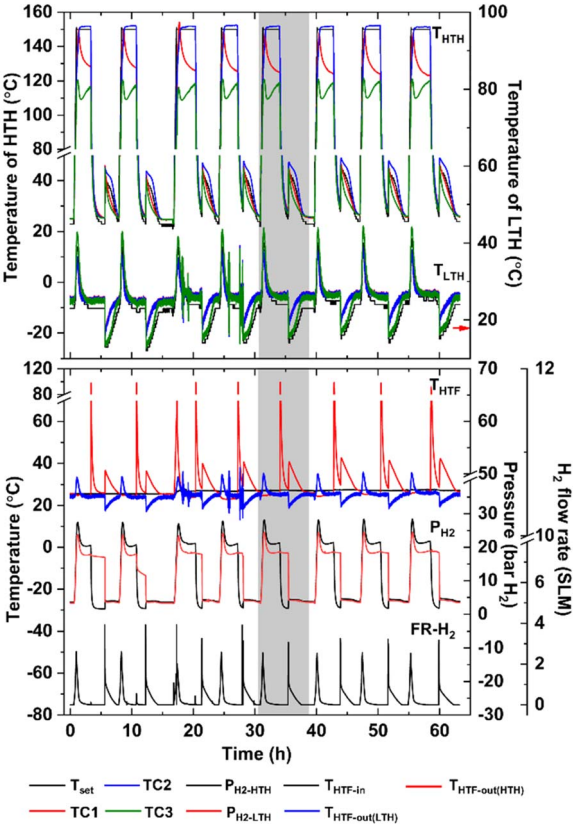

Fig. 5 Temperatures and pressures of the HTH, LTH, and HTF as well as the hydrogen mass flow rate upon 8 heat charging and discharging cycles of coupled $LaNi_5$–$La_{0.6}Ce_{0.4}Ni_5$.

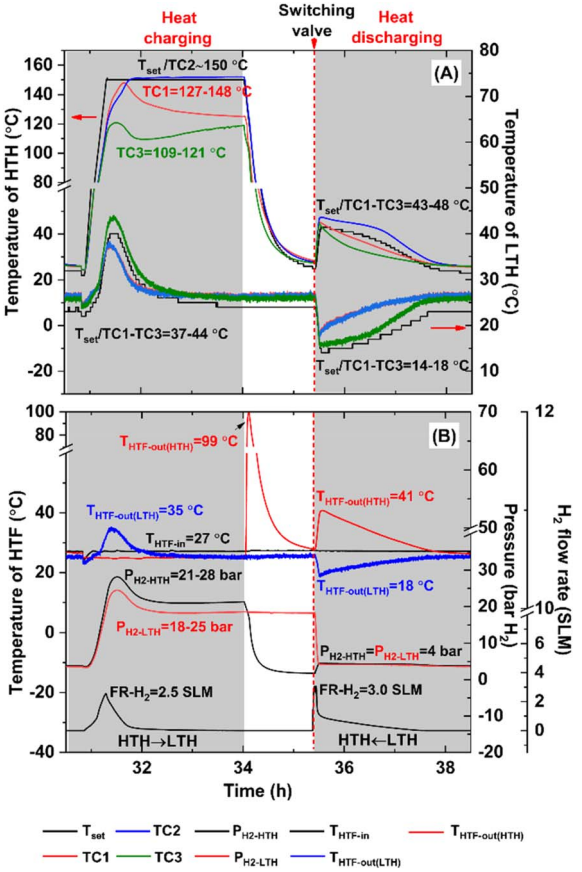

Fig. 6 Temperatures of HTH and LTH (A) and pressures, hydrogen mass flow rate, and temperature of HTF (B) during the 5th heat charging and discharging cycle of coupled $LaNi_5$–$La_{0.6}Ce_{0.4}Ni_5$.

h) and reduction in temperature at TC1 and TC3 (t = 31.5–32 h). The hydrogen gas desorbed from HTH migrates to LTH, in accordance with the enhancement in H_2-FR to 2.5 SLM as well as $P_{H_2\text{-HTH}}$ and $P_{H_2\text{-LTH}}$ to 21–28 and 18–25 bar H_2, respectively (Fig. 6(B)). Exothermic hydrogenation of LTH results in an increase in the sample temperature in the LTH tank (TC1–TC3) from room temperature (25–27 °C) to 37–44 °C (Fig. 6(A)). Meanwhile, deionized water used as the heat transfer fluid (HTF) delivered the heat generated during the hydrogenation of LTH ($T_{\text{HTF-out(LTH)}}$ = 35 °C). The heat charge process was complete within ~2 h (t = 33 h), as confirmed by the temperature reduction of LTH (TC1–TC3) and HTF ($T_{\text{HTF-out(LTH)}}$) to room temperature. According to the dehydrogenation enthalpy and entropy of HTH of 27.3 kJ mol^{-1} and 96.5 J K^{-1} mol^{-1}, respectively (Fig. 4) and the Van't Hoff equation (eqn (6)), the calculated P_{eq} upon hydrogen desorption from HTH at 109–150 °C detected at TC-TC3 (Fig. 6(A)) is 20.0–46.7 bar H_2. In the case of LTH, P_{eq} upon hydrogen absorption on $La_{0.4}Ce_{0.6}Ni_5$ at 40 °C was ~30 bar H_2.[32] These values are in accordance with our results that dehydrogenation of HTH leads to $P_{H_2\text{-HTH}}$ of up to 28 bar H_2, and hydrogenation of LTH ($La_{0.6}Ce_{0.4}Ni_5$-2wt% MWCNTs) at room temperature (~25–27 °C) can be accomplished at $P_{H_2\text{-LTH}}$ = 25 bar H_2 (Fig. 6(B)). During t = 31–32 h, exothermic hydrogenation of LTH proceeded rapidly due to the sufficient pressure, resulting in a significant enhancement in FR-H_2 = 2.5 SLM, TC1-TC3 of LTH = 37–44 °C, and $T_{\text{HTF-out(LTH)}}$ = 35 °C (Fig. 6). Afterward (t = 32–34 h), FR-H_2, TC1–TC3 of LTH, and $T_{\text{HTF-out(LTH)}}$ decreased drastically. These results indicate that hydrogen absorption at LTH is impeded due to the reduction in supplied pressure ($P_{H_2\text{-LTH}}$ = 18 bar H_2). Meanwhile, the high back pressure at HTH ($P_{H_2\text{-HTH}}$ = 21 bar H_2) probably slows down its hydrogen desorption.

When heat charge finished, HTH and LTH were disconnected, and HTH was cooled to room temperature using HTF (t = 34–35 h). The latter resulted in an enhanced $T_{\text{HTF-out(HTH)}}$ from ~25 °C to 90 °C and reduced $P_{H_2\text{-HTH}}$ from 21.0 to ~1.0 bar H_2 (Fig. 6(B)). Heat discharge begins with the release of hydrogen from LTH at room temperature to HTH, corresponding to an increase in FR-H_2 to 3.0 SLM. Endothermic dehydrogenation occurs at LTH, shown as the temperature reduction of LTH (TC1–TC3) and HTF from room temperature (~25 °C) to 14–18 °C and 18 °C, respectively (Fig. 6). Meanwhile, exothermic hydrogenation at HTH leads to the elevated temperatures of HTH and HTF to 43–48 °C and 41 °C, respectively. The heating and cooling effects detected during the heat discharge of the coupled $LaNi_5$–$La_{0.6}Ce_{0.4}Ni_5$ were revealed as an increase and decrease in the HTF temperatures at HTH (ΔT = 16 °C) and LTH (ΔT = 7 °C), respectively. At ~25–30 °C, P_{eq} during dehydrogenation of LTH was 7.7 bar H_2 (Fig. 3), and P_{eq}

during the hydrogenation of $LaNi_5$ was about 3 bar H_2.[31] According to Fig. 6(B), $P_{H_2\text{-HTH}}$ and $P_{H_2\text{-LTH}}$ of 4.0 bar H_2 are comparable and between P_{eq} during the dehydrogenation of LTH and hydrogenation of HTH ($LaNi_5$-2 wt% MWCNTs). This encourages their hydrogen exchange reaction. It should be noted that during heat discharge, not only heat from HTH up to 41 °C ($\Delta T = 16$ °C) is delivered by HTF but also coolness from LTH at the lowest temperature of 18 °C ($\Delta T = 7$ °C) (Fig. 6(B)). At the comparable charging temperature of 150 °C, the heating and cooling effects obtained from our study are significantly superior to that of the $LaNi_{4.25}Al_{0.75}$-$La_{0.75}Ce_{0.25}Ni_5$ pair ($\Delta T =$ 7.3 °C and 2.4 °C, respectively).[15] Heat discharge was completed within about 2 h ($t \sim 37.5$ h). Given that the thermodynamics and hydrogen ab/desorption kinetics of HTH and LTH are compatible, the time for the heat charge and discharge processes was equal (~2 h). This probably favors the design of the coupled $LaNi_5$–$La_{0.4}Ce_{0.6}Ni_5$ thermal storage system for practical utilization given that an extra unit of HTH or LTH is not required to optimize the heat charge and discharge rates.

Furthermore, the gravimetric and volumetric energy densities (Q_g and Q_v, respectively) during heat charge and discharge of the coupled $LaNi_5$–$La_{0.4}Ce_{0.6}Ni_5$ were calculated using the reaction enthalpy and the moles of hydrogen exchanged between HTH and LTH (eqn (8) and (9), respectively).[19,45,46] According to Fig. 7(A) and Table 3, the moles of hydrogen exchanged between HTH and LTH upon 8 heat charge and discharge cycles are 2.69 ± 0.03 and 2.65 ± 0.05 mol H_2, respectively. With respect to the weight of the powder samples in the HTH or LTH container (0.6 kg), these moles of hydrogen correspond to the storage capacities of 0.90 ± 0.01 and 0.89 ± 0.02 wt% H_2, respectively. These hydrogen capacities are considerably greater than that of the coupled $LaNi_{4.25}Al_{0.75}$-$La_{0.75}Ce_{0.25}Ni_5$ (0.42 wt% H_2) at the comparable charging temperature of 150 °C.[15] The calculated gravimetric and volumetric energy densities during heat charge are 122.40 ± 1.37 kJ kg^{-1} and 60.00 ± 0.65 kW h m^{-3}, while that during heat discharge are 120.60 ± 2.30 kJ kg^{-1} and 57.10 ± 1.10 kW h m^{-3}, respectively (Table 3). The consistent moles of hydrogen exchanged between HTH and LTH indicate the cycling stability of the coupled $LaNi_5$–$La_{0.6}Ce_{0.4}Ni_5$ upon cycling. The obtained volumetric and gravimetric energy densities of the coupled $LaNi_5$–$La_{0.6}Ce_{0.4}Ni_5$ from our study (up to 122 kJ kg^{-1} and 60 kW h m^{-3}, respectively) are comparable to that of the coupled $LaNi_{4.65}Sn_{0.35}$-$MmNi_{4.6}Al_{0.4}$ (129 kJ kg^{-1})[30] and $LaNi_{4.7}Al_{0.3}$-$LaNi_5$ (56 kW h m^{-3}).[29]

$$Q_g = \frac{n_{H_2}\Delta H_R}{m_{HTH}} \quad (8)$$

$$Q_v = \frac{n_{H_2}\Delta H_R}{V_p} \quad (9)$$

where n_{H_2}, ΔH_R, and m_{HTMH} are moles of hydrogen exchanged between HTH and LTH during heat charge and discharge, reaction enthalpy of HTH (27.3 kJ per mol H_2 or 7.58 W h per mol H_2 according to Fig. 4 and Table 2), and mass of HTH powder sample (0.60 kg), respectively. V_p is a packing volume of the HTH container (3.5×10^{-4} m^3).

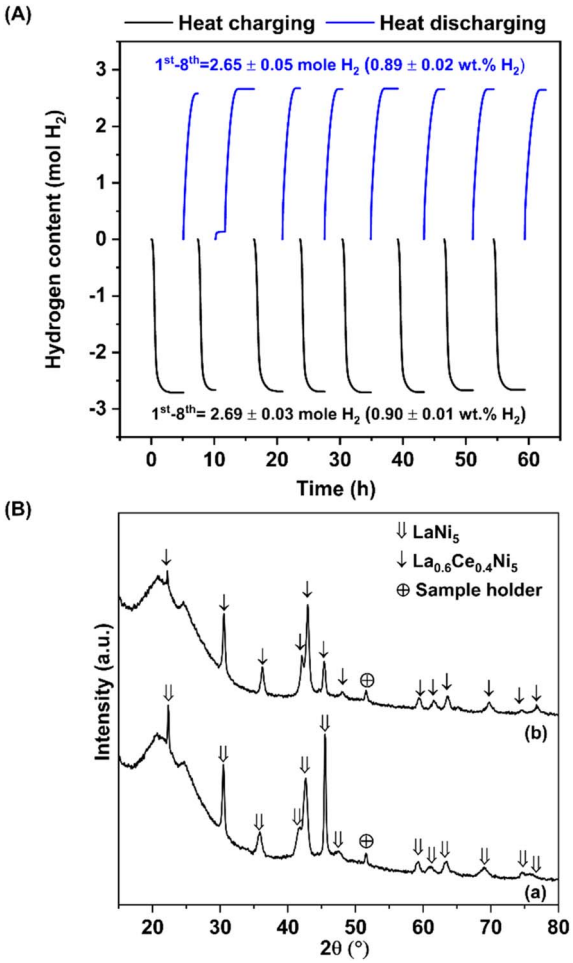

Fig. 7 Hydrogen contents exchange between HTH and LTH upon 8 heat storage cycles (A) and PXD patterns of HTH (a) and LTH (b) after cycling (B) of coupled $LaNi_5$–$La_{0.6}Ce_{0.4}Ni_5$.

Compared to the full hydrogen capacities of HTH and LTH of 1.23 and 1.07 wt% H_2, respectively (Fig. 2(B) and Table 2), the hydrogen content participating in the heat exchange reaction is up to 73% and 84% of the full capacities of HTH and LTH, respectively. This deficient hydrogen capacity might be attributed to the limited hydrogen content released from HTH and absorbed by LTH during heat charge due to the saturation of hydrogen pressure at t = 32.5–34 h (Fig. 6(B)). This can be explained by the fact that $P_{H_2\text{-HTH}}$ (21 bar H_2) is likely greater than P_{eq} for the dehydrogenation of HTH, while $P_{H_2\text{-LTH}}$ (18 bar H_2) is probably lower than P_{eq} for the hydrogenation of LTH. Thus, the dehydrogenation of HTH and hydrogenation of LTH are limited. The performance and energy densities during heat charge and discharge of the coupled HTH–LTH can be enhanced by selecting hydride pairs with greater ΔP_{eq}. Nevertheless, the latter might lead to the elevated charging temperature of HTH to provide sufficient pressure for hydrogen absorption on LTH. Further studies based on multiple-stage hydrides with compatible P_{eq} and hydrogen de/absorption kinetics should be considered to reduce the charging temperature. After 8 heat charge and discharge cycles, the phase

Table 3 Hydrogen flow direction and hydrogen contents exchange between the HTH and LTH as well as gravimetric and volumetric energy densities during heat charge and discharge

Reactions	H_2 flow direction	Hydrogen moles and capacities exchange between HTH and LTH	Gravimetric energy density (kJ kg^{-1})	Volumetric energy density (kW h m^{-3})
Heat charge	HTH → LTH	2.69 ± 0.03 mol H_2 (0.90 ± 0.10 wt% H_2)	122.40 ± 1.37	60.00 ± 0.65
Heat discharge	HTH ← LTH	2.65 ± 0.05 mol H_2 (0.89 ± 0.02 wt% H_2)	120.60 ± 2.30	57.10 ± 1.10

compositions of HTH and LTH were investigated. According to Fig. 7(B), the diffraction patterns of HTH and LTH show the characteristic peaks of $LaNi_5$ and $La_{0.6}Ce_{0.4}Ni_5$, respectively. Concurrently, the unit cell volumes of HTH and LTH after cycling (86.970 and 85.260 $Å^3$, respectively) were comparable to that of the as-prepared HTH and LTH (Table 1). The maintained diffraction results upon cycling of the HTH and LTH powder samples indicate the stability of these hydrides upon heat charge and discharge cycles. This is in accordance with their preserved hydrogen contents and energy densities upon cycling (Fig. 7(A)).

4. Conclusions

The heat charge and charge performance, mechanisms, and reversibility as well as energy densities of the coupled $LaNi_5$–$La_{0.6}Ce_{0.4}Ni_5$ were investigated. $LaNi_5$ with a lower equilibrium pressure and higher reaction enthalpy was used as a high-temperature hydride (HTH) for heat storage, while $La_{0.6}Ce_{0.4}Ni_5$ acted a low-temperature hydride (LTH) and hydrogen reservoir. MWCNTs (2 wt%) were added to HTH and LTH for enhancing the thermal conductivity and hydrogen diffusion in the hydride beds. The powder samples were packed into the two connected cylindrical containers mounted with a spiral heat exchanger. The sample mass and the packing volume of each container were 0.6 kg and 0.35 L, respectively. During heat charge at 150 °C, the obtained hydrogen pressure at HTH of up to 28 bar was sufficient to accelerate hydrogen absorption on LTH. In the case of discharge, LTH with a higher P_{eq} released hydrogen up to 4 bar at room temperature and HTH concurrently reabsorbed the hydrogen. The heating and cooling effects achieved during energy discharge were observed from the elevated and reduced temperatures of the heat transfer fluid at HTH ($\Delta T = 16$ °C) and LTH ($\Delta T = 7$ °C), respectively. According to the compatible thermodynamics and kinetics of these hydrides, the reaction times during heat charge and discharge were comparable at ~2 h. The gravimetric and volumetric energy densities during heat charge were 122.40 ± 1.37 kJ kg^{-1} and 60.0 ± 0.65 k Wh m^{-3}, while that during heat discharge were 120.60 ± 2.30 kJ kg^{-1} and 57.10 ± 1.10 kW h m^{-3}, respectively. The phase compositions of both hydrides were preserved upon 8 heat storage cycles, and the hydrogen contents exchanged between HTH and LTH of ~2.70 mol H_2 or 0.9 wt% H_2 were consistent. These results indicated the cycling stability of the coupled $LaNi_5$–$La_{0.6}Ce_{0.4}Ni_5$ thermal storage system.

Data availability

The data supporting this article have been included as part of the ESI† and are available from the corresponding author (Dr Rapee Utke) upon reasonable request.

Author contributions

Praphatsorn Plerdsranoy: conceptualization, sample preparation, characterizations, data analysis, and manuscript writing. Chonticha Hansongkram: characterizations, data analysis, and manuscript writing. Suwabun Chirachanchai: funding acquisition, supervision, resources, reviewing and editing. Rapee Utke: conceptualization, supervision, funding acquisition, resources, data analysis, validation, manuscript writing, reviewing and editing.

Conflicts of interest

There are no conflicts to declare.

Acknowledgements

Rapee Utke and Praphatsorn Plerdsranoy would like to acknowledge Suranaree University of Technology for research funding. Suwabun Chirachanchai appreciates the support from the National Research Council of Thailand (NRCT) [grant number: N42A640322].

References

1 A. Palacios, C. Barreneche, M. E. Navarro and Y. Ding, *Renewable Energy*, 2020, **156**, 1244–1265.
2 I. Sarbu and C. Sebarchievici, *Sustainability*, 2018, **10**, 191.
3 C. Suresh and R. P. Saini, *Int. J. Energy Res.*, 2020, **44**, 4163–4195.
4 A. Gil, M. Medrano, I. Martorell, A. Lázaro, P. Dolado, B. Zalba and L. F. Cabeza, *Renewable Sustainable Energy Rev.*, 2010, **14**, 31–55.
5 M. Medrano, A. Gil, I. Martorell, X. Potau and L. F. Cabeza, *Renewable Sustainable Energy Rev.*, 2010, **14**, 56–72.

6 P. Pardo, A. Deydier, Z. Anxionnaz-Minvielle, S. Rougé, M. Cabassud and P. Cognet, *Renewable Sustainable Energy Rev.*, 2014, **32**, 591–610.
7 D. Aydin, S. P. Casey and S. Riffat, *Renewable Sustainable Energy Rev.*, 2015, **41**, 356–367.
8 D. A. Sheppard, M. Paskevicius, T. D. Humphries, M. Felderhoff, G. Capurso, J. Bellosta von Colbe, M. Dornheim, T. Klassen, P. A. Ward, J. A. Teprovich, C. Corgnale, R. Zidan, D. M. Grant and C. E. Buckley, *Appl. Phys. A:Mater. Sci. Process.*, 2016, **122**, 1–15.
9 B. C. Mouli, T. J. Tenson, M. S. Choudhari, M. Paswan and V. K. Sharma, *Mater. Today: Proc.*, 2022, **51**, 1521–1526.
10 F. Nie, T. Ma, Q. Zhang, Z. Chang, T. Ren, K. F. Sayfieva, M. Fu and X. Li, *J. Cleaner Prod.*, 2024, **450**, 142003.
11 Y. Tian and C. Y. Zhao, *Appl. Energy*, 2013, **104**, 538–553.
12 B. Li, J. Li, H. Shao and L. He, *Appl. Sci.*, 2018, **8**, 1375.
13 E. C. E. Rönnebro, G. Whyatt, M. Powell, M. Westman, F. Zheng and Z. Z. Fang, *Energies*, 2015, **8**, 8406–8430.
14 D. N. Harries, M. Paskevicius, D. A. Sheppard, T. E. C. Price and C. E. Buckley, *Proc. IEEE*, 2012, **100**, 539–549.
15 K. Malleswararao, P. Kumar, P. Dutta and S. Srinivasa Murthy, *Int. J. Hydrogen Energy*, 2024, **56**, 1371–1383.
16 Z. Z. Fang, C. Zhou, P. Fan, K. S. Udell, R. C. Bowman, J. J. Vajo, J. J. Purewal and B. Kekelia, *J. Alloys Compd.*, 2015, **645**, S184–S189.
17 D. A. Sheppard and C. E. Buckley, *Int. J. Hydrogen Energy*, 2019, **44**, 9143–9163.
18 B. Chandra Mouli, V. K. Sharma, Sanjay, M. Paswan and B. Thomas, *Int. J. Hydrogen Energy*, 2024, **96**, 1203–1214.
19 S. Thiangviriya, P. Thongtan, N. Thaweelap, P. Plerdsranoy and R. Utke, *Int. J. Hydrogen Energy*, 2024, **49**, 59–66.
20 P. Feng, Z. Wu, Y. Zhang, F. Yang, Y. Wang and Z. Zhang, *Appl. Energy*, 2018, **217**, 25–36.
21 P. Feng, Y. Liu, I. Ayub, Z. Wu, F. Yang and Z. Zhang, *Appl. Energy*, 2019, **242**, 148–156.
22 K. Malleswararao, A. N, S. Srinivasa Murthy and P. Dutta, *Int. J. Hydrogen Energy*, 2020, **45**, 16239–16253.
23 S. Tiwari and P. Sharma, *Energy Fuels*, 2022, **36**, 1140–1150.
24 L. Poupin, T. D. Humphries, M. Paskevicius and C. E. Buckley, *Sustainable Energy Fuels*, 2019, **4**, 285–292.
25 A. d'Entremont, C. Corgnale, M. Sulic, B. Hardy, R. Zidan and T. Motyka, *Int. J. Hydrogen Energy*, 2017, **42**, 22518–22529.
26 S. Mellouli, F. Askri, A. Edacherian, T. Alqahtani, S. Algarni, J. Abdelmajid and P. Phelan, *Appl. Therm. Eng.*, 2018, **144**, 1017–1029.
27 D. A. Sheppard, C. Corgnale, B. Hardy, T. Motyka, R. Zidan, M. Paskevicius and C. E. Buckley, *RSC Adv.*, 2014, **4**, 26552–26562.
28 K. Sarath Babu, E. Anil Kumar and S. Srinivasa Murthy, *Appl. Therm. Eng.*, 2023, **219**, 119521.
29 N. Aswin, P. Dutta and S. S. Murthy, *Appl. Therm. Eng.*, 2016, **109**, 949–957.
30 K. S. Babu and E. A. Kumar, *Mater. Today: Proc.*, 2022, **49**, 2042–2047.
31 S. S. Mohammadshahi, E. M. A. Gray and C. J. Webb, *Int. J. Hydrogen Energy*, 2016, **41**, 3470–3484.
32 P. Hannappel, F. Heubner, M. Balcerzak and T. Weißgärber, *Acta Mater.*, 2025, **284**, 120529.
33 L. Popilevsky, V. M. Skripnyuk, Y. Amouyal and E. Rabkin, *Int. J. Hydrogen Energy*, 2017, **42**, 22395–22405.
34 C. Sitthiwet, P. Plerdsranoy, P. Dansirima, P. Eiamlamai, O. Utke and R. Utke, *J. Alloys Compd.*, 2020, **832**, 155026.
35 S. Thiangviriya, P. Plerdsranoy, C. Sitthiwet, P. Dansirima, P. Thongtan, P. Eiamlamai, O. Utke and R. Utke, *Int. J. Hydrogen Energy*, 2019, **44**, 20173–20182.
36 P. Dansirima, A. Pangon, O. Utke and R. Utke, *Int. J. Hydrogen Energy*, 2022, **47**, 7351–7361.
37 P. Plerdsranoy and R. Utke, *Int. J. Hydrogen Energy*, 2024, **77**, 582–588.
38 P. Plerdsranoy and R. Utke, *Int. J. Hydrogen Energy*, 2025, **101**, 482–489.
39 G. R. de Almeida Neto, C. A. Gonçalves Beatrice, D. R. Leiva and L. A. Pessan, *Int. J. Hydrogen Energy*, 2020, **45**, 14017–14027.
40 M. Pęska, J. Dworecka-Wójcik, T. Płociński and M. Polański, *Energies*, 2020, **13**, 1437.
41 W. liang Mi, Z. sen Liu, T. Kimura, A. Kamegawa and H. liang Wang, *Int. J. Miner., Metall. Mater.*, 2019, **26**, 108–113.
42 A. Züttel, *Mater. Today*, 2003, **6**, 24–33.
43 E. Hahne and J. Kallweit, *Int. J. Hydrogen Energy*, 1998, **23**, 107–114.
44 D. min Kim, J. B. Kim, J. Lee and B. J. Lee, *Int. J. Heat Mass Transfer*, 2021, **165**, 120735.
45 R. Urbanczyk, M. Meggouh, R. Moury, K. Peinecke, S. Peil and M. Felderhoff, *Appl. Phys. A:Mater. Sci. Process.*, 2016, **122**, 1–5.
46 R. Urbanczyk, K. Peinecke, S. Peil and M. Felderhoff, *Int. J. Hydrogen Energy*, 2017, **42**, 13818–13826.